

CONSTRAINING THE POROSITIES OF INTERSTELLAR DUST GRAINS

KEVIN HENG¹ & BRUCE T. DRAINE²*Draft version June 4, 2009*

ABSTRACT

We present theoretical calculations of the X-ray scattering properties of porous grain aggregates with olivine monomers. The small and large angle scattering properties of these aggregates are governed by the global structure and substructure of the grain, respectively. We construct two diagnostics, \mathcal{R}_X and \mathcal{T}_X , based on the optical and X-ray properties of the aggregates, and apply them to a *Chandra* measurement of the dust halo around the Galactic binary GX13+1. Grain aggregates with porosities $\mathcal{P} \gtrsim 0.55$ are ruled out. Future high-precision observations of X-ray dust haloes together with detailed modeling of the X-ray scattering properties of porous grain mixtures will further constrain the presence of porous grain aggregates in a given dust population.

Subject headings: ISM: dust, extinction — scattering — X-rays: diffuse background

1. INTRODUCTION

After many decades of trying to deduce the properties of interstellar dust from observations, the basic geometric structure of the grains remains controversial. The observed polarization of starlight establishes that some or all grains are non-spherical, and there is agreement that interstellar grains must include both silicate material and carbonaceous material, but there are divergent views concerning the internal structure of grains. Some authors (e.g., Mathis et al. 1977; Draine & Lee 1984; Kim, Martin & Hendry 1994; Kim & Martin 1995; Weingartner & Draine 2001, hereafter WD01; Draine & Li 2007; Draine & Fraisse 2009) have modeled interstellar grains as compact, zero-porosity spheres or spheroids, with some consisting of silicate and others consisting of carbonaceous material. Others have argued that the evolution of interstellar grains involves coagulation in clouds, producing grains with a mixed composition and a “fluffy” structure, with porosities taken to be ~ 0.8 (Mathis & Whiffen 1989) or $\gtrsim 0.9$ (Voshchinnikov et al. 2006).

Because polarized light-scattering is sensitive to the geometry of the scatterers, it has been possible to use the observed color and polarization of scattered light, as a function of scattering angle, to estimate the size and porosity of cometary dust particles and the dust in debris disks. Shen et al. (2008, hereafter SDJ08) examined the optical properties of porous grain aggregates using the discrete dipole approximation (Draine 1988; Draine & Flatau 1994). Shen et al. (2009) found that moderate-porosity aggregates can reproduce the observed scattering properties of dust in the AU Mic debris disk and in comets. Unfortunately, the scattering properties of interstellar grains remain uncertain,

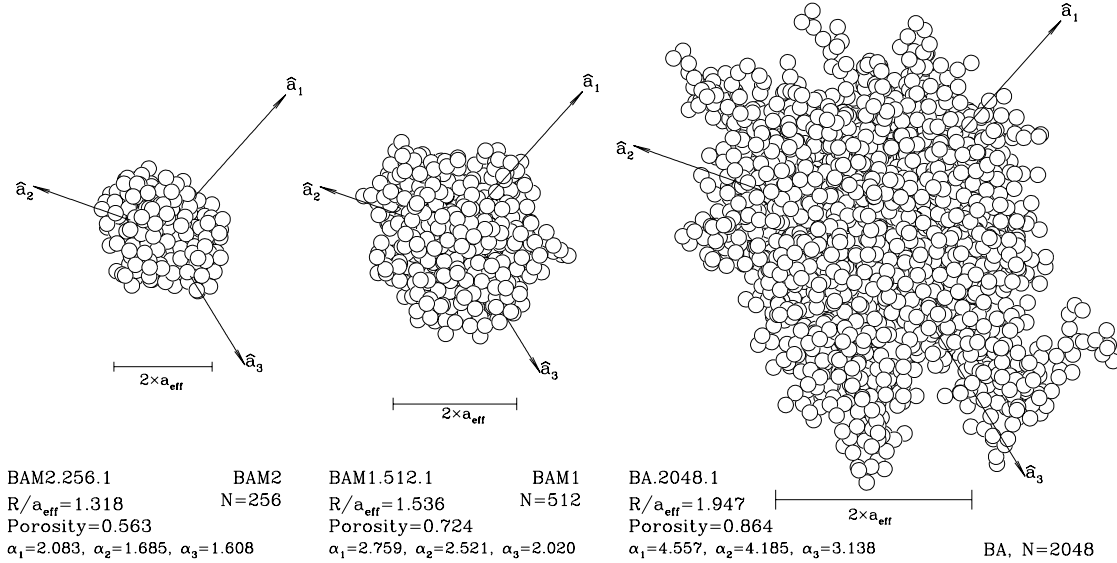


FIG. 1.— Random aggregates produced by the BAM2, BAM1, and BA agglomeration schemes (Shen, Draine & Johnson 2008). The unit vector \hat{a}_1 is along the principal axis of the largest moment of inertia. With $a_0 = 0.04\mu\text{m}$ silicate spherules, each of these aggregates (with $a_{\text{eff}} = 0.254, 0.320, \text{ and } 0.508\mu\text{m}$) has $Q_{\text{ext}}(B)/Q_{\text{ext}}(R) \approx 1.70$, the observed value of A_B/A_R (see text).

¹ Institute for Advanced Study, School of Natural Sciences, Einstein Drive, Princeton, NJ 08540; heng@ias.edu

² Princeton University Observatory, Peyton Hall, Princeton, NJ 08544; draine@astro.princeton.edu

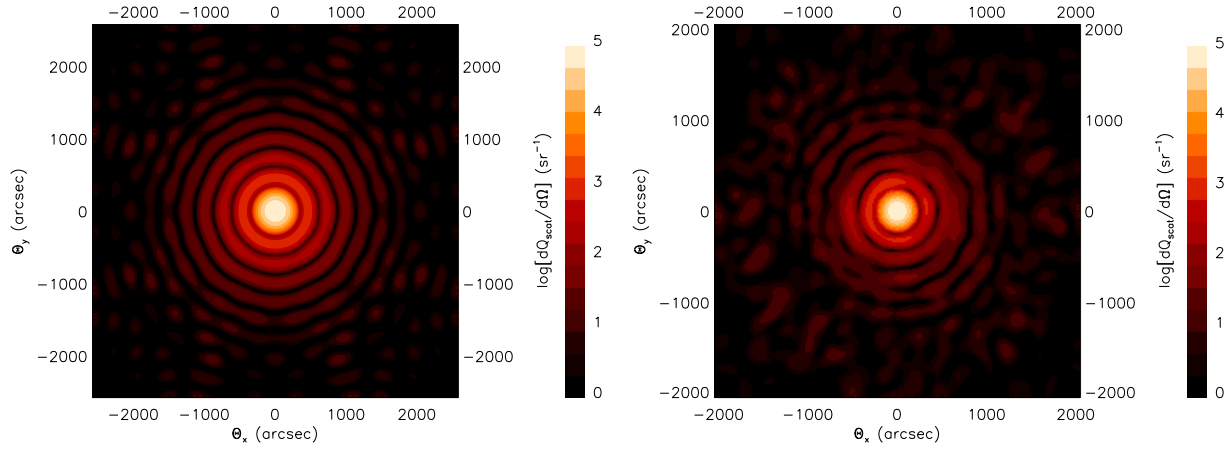


FIG. 2.— Plots of $dQ_{\text{scat}}/d\Omega$ ($E = 2$ keV) for (left) a single spherical grain with radius $a = 0.25 \mu\text{m}$; and (right) the BAM2 aggregate of Fig. 1, with 256 $a_0 = 0.04 \mu\text{m}$ silicate spherules ($\mathcal{P} = 0.563$, $a_{\text{eff}} \approx 0.254 \mu\text{m}$), oriented with $\theta = 0^\circ$, after “ β -averaging” (see text).

and to date there has been no observational diagnostic capable of discriminating between these different models for interstellar grains.

The present study shows that X-ray scattering can discriminate between compact and fluffy models for interstellar dust. Compact grain models have been successful in reproducing observations of X-ray scattering halos (e.g., Draine & Tan 2003, Smith 2008). In the present paper, we show how the X-ray scattering properties of irregular porous grains can be accurately calculated. We find that compact and fluffy grains differ substantially in their X-ray scattering properties, because the X-rays can “see” the small-scale structure within an aggregate grain, and because fluffy grains must be larger than compact grains when required to reproduce observed interstellar reddening constraints.

In §2, we describe the X-ray optics of grain aggregates, including approximate scaling laws and our application of anomalous diffraction theory (ADT) to calculate their X-ray scattering properties. We present the results of our calculations in §3. In §4, we construct two diagnostics based on the optical and X-ray properties of the dust grains and apply them to the *Chandra* halo measurement around the Galactic binary GX13+1 by Smith (2008, hereafter S08). We are able to rule out grain aggregate models with porosities $\mathcal{P} \gtrsim 0.55$. We summarize and discuss our results in §5.

2. X-RAY OPTICS OF GRAIN AGGREGATES

2.1. Anomalous Diffraction Theory (ADT)

ADT, a combination of ray-tracing optics and Huygens’ principle of propagation (van de Hulst 1957), is applicable to the study of dust grains at X-ray energies, when the refractive index is nearly unity and the grain size is relatively large (van de Hulst 1957):

$$\begin{aligned} |m - 1| &\ll 1, \\ k_0 a &\gg 1, \end{aligned} \tag{1}$$

where m is the complex refractive index, $\lambda_0 = 2\pi/k_0$ is the wavelength of the incident photon and a is the size of the dust grain. Draine & Allaf-Akbari (2006, hereafter DA06) applied the ADT to calculate X-ray scattering from non-spherical grains. The interested reader is referred to DA06 or chapter 10 of van de Hulst (1957) for more details.

Let $\mathbf{k}_i = (0, 0, k_0)$ and $\mathbf{k}_s = (k_x, k_y, \sqrt{k_0^2 - k_x^2 - k_y^2})$ be the incident and scattered propagation vectors. The differential scattering cross section is given by

$$\frac{d\sigma_{\text{scat}}}{d\Omega} = \frac{|\mathcal{S}|^2}{k_0^2}, \tag{2}$$

where the scattering function,

$$\mathcal{S}(k_x, k_y; k_0) = k_0^2 \mathcal{F}\{f(x, y; k_0)\}, \tag{3}$$

is related to the Fourier transform of the shadow function, $f = f(x, y; k_0)$:

$$\mathcal{F}\{f\} \equiv \int \exp[i(k_x x + k_y y)] f \, dx dy. \tag{4}$$

The shadow function quantifies the fractional change in the propagating electric field, approximated as a plane wave, at a plane located just beyond the grain:

$$f(x, y; k_0) = 1 - \exp\left[ik_0 \int (m - 1) \, dz\right], \tag{5}$$

where $m = m(x, y, z)$ in general.

2.2. Scaling Laws

We define the “effective radius” (or “volume equivalent radius”),

$$a_{\text{eff}} \equiv \left(\frac{3V}{4\pi} \right)^{1/3}, \quad (6)$$

where V is the volume of solid material in the grain. If \mathcal{P} is the grain porosity as defined by SDJ08, then the characteristic size is

$$R \equiv a_{\text{eff}}(1 - \mathcal{P})^{-1/3}. \quad (7)$$

The grain is assumed to be made up of N_s spherical monomers (“spherules”) with radii a_0 such that $a_{\text{eff}} = N_s^{1/3} a_0$. The porosity $\mathcal{P} = \mathcal{P}(N_s)$, depends on the agglomeration scheme used (see §3). In Fig. 1, we show visualizations of three random aggregates.

Consider an X-ray photon with wave number k_0 encountering a dust grain and deflected by an angle Θ and a transverse wave number, $k_{\perp} = k_0 \sin \Theta$. The characteristic scattering angle is

$$\begin{aligned} \Theta_{\text{char}} &\equiv \frac{2}{k_0 R} = \frac{\lambda_0}{\pi R} \\ &= 271'' (1 - \mathcal{P})^{1/3} \left(\frac{1 \text{ keV}}{E} \right) \left(\frac{0.3 \mu\text{m}}{a_{\text{eff}}} \right). \end{aligned} \quad (8)$$

The total scattering cross section is

$$\sigma_{\text{scat}} \approx \left(\frac{d\sigma_{\text{scat}}}{d\Omega} \right)_{\Theta=0} \pi \Theta_{\text{char}}^2. \quad (9)$$

We can derive approximate scaling laws for $d\sigma_{\text{scat}}/d\Omega$ at small and large angles. At sufficiently high energies such that $|f| \ll 1$, we have

$$\mathcal{F}\{f\} \approx \sum_j \exp(i\phi_j) \mathcal{F}_0, \quad (10)$$

where \mathcal{F}_0 is the Fourier transform of the shadow function for one spherule and ϕ_j is the phase contribution by the j -th spherule.

At small scattering angles ($k_{\perp} R \lesssim 1$; “core”), we have $\mathcal{F}_0 \approx -ik_0(m-1)V_0$ where $V_0 = 4\pi a_0^3/3$ is the volume of one spherule. The phase shifts are small ($\langle \phi_j^2 \rangle \lesssim 1$) and coherent scattering occurs:

$$\mathcal{F} \approx N_s \mathcal{F}_0. \quad (11)$$

It follows that

$$\frac{d\sigma_{\text{scat}}}{d\Omega} \approx (N_s V_0 k_0^2)^2 |m-1|^2. \quad (12)$$

At large scattering angles ($k_{\perp} R \gg 1$; “wing”), the phase shifts are large and pseudo-random so that

$$|\mathcal{F}| \approx N_s^{1/2} |\mathcal{F}_0|. \quad (13)$$

To evaluate \mathcal{F}_0 , we examine the scattering function for a single spherule (van de Hulst 1957):

$$\mathcal{S}_0(\Theta; k_0) = (k_0 a_0)^2 \int_0^{\pi/2} [1 - \exp(-i\rho \sin u)] \mathcal{J}_0(\chi \cos u) \sin u \cos u \, du, \quad (14)$$

where $\rho \equiv 2k_0 a_0(m-1)$, $\chi \equiv k_0 a_0 \Theta$ and \mathcal{J}_0 is the zeroth order Bessel function. When $\chi \gg 1$ and $\rho \sim 1$,

$$\begin{aligned} \mathcal{S}_0(\Theta; k_0) &\approx i \left(\frac{\pi}{2} \right)^{1/2} (k_0 a_0)^2 \rho \chi^{-3/2} \mathcal{J}_{3/2}(\chi) \\ &\approx 2i(m-1) k_0 a_0 \Theta^{-2}, \end{aligned} \quad (15)$$

since (Arfken & Weber 1995)

$$\mathcal{J}_l(\chi) \approx \sqrt{\frac{2}{\pi\chi}} \cos \left[\chi - \frac{\pi}{2} \left(l + \frac{1}{2} \right) \right] \quad (16)$$

for $\chi \gg 1$. We then have

$$\frac{d\sigma_{\text{scat}}}{d\Omega} \approx 4N_s |m-1|^2 a_0^2 \Theta^{-4} = 4|m-1|^2 \left(\frac{a_{\text{eff}}^3}{a_0} \right) \Theta^{-4}. \quad (17)$$

The scattering at large angles is proportional to the “power” at large k_{\perp} in $|\mathcal{F}(f)|^2$.

Consequently, the normalized differential scattering cross section follows the scaling laws:

$$\frac{dQ_{\text{scat}}}{d\Omega} \equiv \frac{1}{\pi a_{\text{eff}}^2} \frac{d\sigma_{\text{scat}}}{d\Omega} \propto \begin{cases} N_s^{4/3} & , \Theta \ll \Theta_{\text{char}}, \\ N_s^{1/3} \Theta^{-4} & , \Theta \gg \Theta_{\text{char}}. \end{cases} \quad (18)$$

We expect these scaling laws to be obeyed when absorption effects are weak:

$$\tau \equiv k_0 a_{\text{eff}} m_i (1 - \mathcal{P})^{2/3} \ll 1, \quad (19)$$

where m_i is the imaginary part of the index of refraction. For $E \geq 1$ keV, we have $m_i \leq 1.9 \times 10^{-4}$ for olivine (MgFeSiO_4) and thus $\tau \leq 0.3(1 - \mathcal{P})^{2/3}$ for $a_{\text{eff}} = 0.3 \mu\text{m}$.

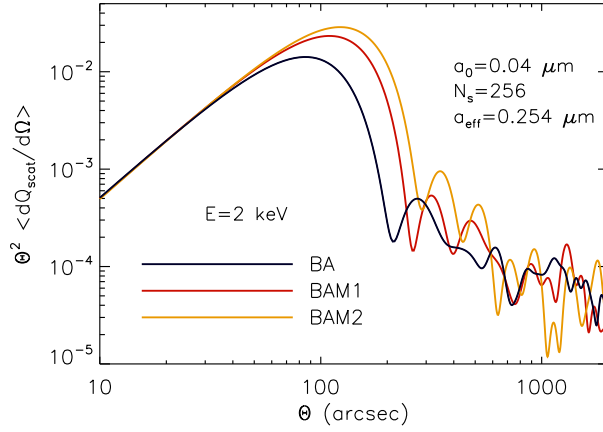


FIG. 3.— $\langle dQ_{\text{scat}}/d\Omega \rangle$ at $E = 2$ keV as a function of the scattering angle, Θ , for BA.256.1 ($\mathcal{P} = 0.860$), BAM1.256.1 ($\mathcal{P} = 0.706$) and BAM2.256.1 ($\mathcal{P} = 0.563$) aggregates, each consisting of 256 $a_0 = 0.04 \mu\text{m}$ silicate spherules.

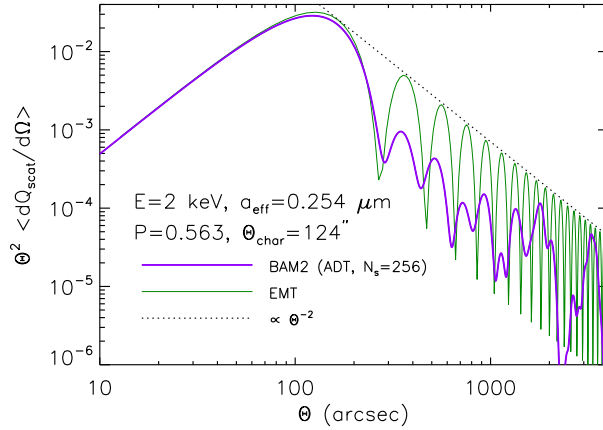


FIG. 4.— Comparing ADT and EMT calculations for $\langle dQ_{\text{scat}}/d\Omega \rangle$ at $E = 2$ keV for BAM2.256.1 with $a_0 = 0.04 \mu\text{m}$.

2.3. Implementation

To calculate the differential scattering cross section in equation (2), we adapt the **Fortran 90** routine `four2.f90` from Press et al. (1996) for computing two-dimensional fast Fourier transforms (FFTs) with complex input functions. We are able to reproduce all of the results in Fig. 1 of DA06, thus verifying the accuracy of our code. As in the case of DA06, we find that a square, cartesian grid (x, y) with $(2^{11})^2$ to $(2^{12})^2$ points suffices for our purposes and avoids spurious contributions to the FFT resulting from aliasing. Bilinear interpolation is used to map the calculations into polar coordinates.

3. RESULTS

SDJ08 studied three types of grain aggregate models with different ranges of porosities. The most porous grains are the BA (“ballistic agglomeration”) aggregates, constructed by requiring the arriving monomers to adhere to the point where they first made contact with the pre-existing aggregate. Less porous are the BAM1 (“BA with one migration”) aggregates, where an arriving monomer is required to roll or slide along the contacted monomer, via the shortest possible trajectory, until a second contact point is established with the aggregate. The most compact aggregates are the BAM2 (“BA with two migrations”). For $256 \leq N_s \leq 4096$, the BA, BAM1 and BAM2 aggregates have $\langle \mathcal{P} \rangle \approx 0.85$ – 0.86 , 0.74 – 0.78 and 0.58 – 0.66 , respectively (see Table 2 of SDJ08). The current study employs random realizations of BA, BAM1, and BAM2 aggregates.³ The monomers are assumed to have composition MgFeSiO_4 and density $\rho = 3.8 \text{ g cm}^{-3}$ of olivine, with refractive index from Draine (2003).

The orientation of each aggregate is defined by two angles: θ is the angle between the line of sight and the principal axis of the largest moment of inertia, with unit vector \hat{a}_1 ; and β is the rotation angle about \hat{a}_1 . Rotation of \hat{a}_1 about

³ Available in electronic form at <http://www.astro.princeton.edu/~draine/agglom.html>.

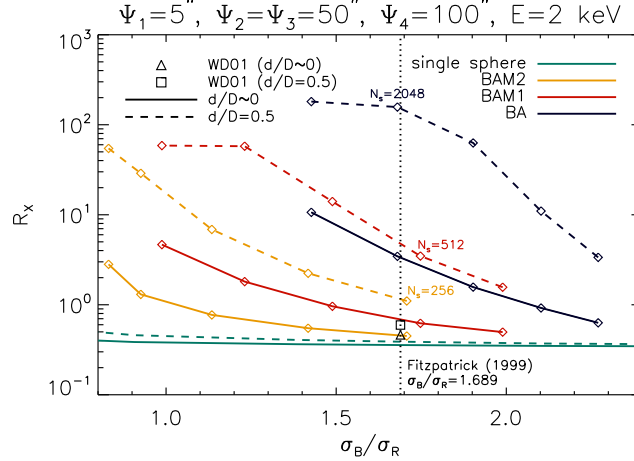


FIG. 5.— \mathcal{R}_X vs. the ratio of B - to R -band extinction cross sections. Higher \mathcal{R}_X and lower σ_B/σ_R values correspond to larger grain sizes. We have considered grain aggregates consisting of $N_s = 256, 512, 1024, 2048$ and 4096 silicate spherules with radii $a_0 = 0.04 \mu\text{m}$. For comparison, calculations for single silicate spheres are shown. Also shown is the X-ray halo calculated for the WD01 mixture of silicate and carbonaceous grains. The dotted vertical line is $\sigma_B/\sigma_R = 1.689$ observed for typical diffuse cloud sightlines with $A_V/E(B-V) \approx 3.1$ (Fitzpatrick 1999).

the line of sight can be suppressed because the scattered intensity will later be azimuthally averaged. Because of the reflection symmetry of the shadow function, we need to calculate \mathcal{S} only for $0 \leq \theta \leq \pi/2$ and $0 \leq \beta \leq \pi$. For 11 values of θ , we average $dQ_{\text{scat}}/d\Omega$ over 11 values of β (“ β -averaging”).

We compute $dQ_{\text{scat}}/d\Omega$ for the BAM2.256.1 aggregate with $N_s = 256$ in the right panel of Fig. 2. The effective radius for this grain aggregate is $a_{\text{eff}} = 0.254 \mu\text{m}$ ($R \approx 0.335 \mu\text{m}$). For comparison, we calculate $dQ_{\text{scat}}/d\Omega$ for a solid sphere with $a = 0.25 \mu\text{m}$. The first feature to notice is the series of distinct rings in the case of the solid sphere. These are the two-dimensional analogue of the Fourier transform of a Heaviside function in one dimension, and are artifacts of the sharply-defined edge of the spherical grain. For the aggregate, traces of these rings persist, but they are smeared out because there is no sharp spherical outer edge.

Secondly, the scattering has similar intensities for both the spherical grain and the grain aggregate, but the central peak is concentrated within a smaller angular area for the latter. This is a simple consequence of the fact that porous grains generally have larger characteristic sizes than solid spheres. Larger grain sizes result in more concentrated forward scattering.

For the rest of the paper, we average $dQ_{\text{scat}}/d\Omega$ over 11 values of the orientation angle θ (“ θ -averaging”). We also define $\langle dQ_{\text{scat}}/d\Omega \rangle$ to be the azimuthal average of the two-dimensional $dQ_{\text{scat}}/d\Omega$ function. We show examples of $\langle dQ_{\text{scat}}/d\Omega \rangle$ for $N_s = 256$ aggregates with BA, BAM1 and BAM2 porosities in Fig. 3. As expected from equation (12), the BA, BAM1, and BAM2 aggregates have nearly identical forward scattering, but the BA clusters, being “larger”, have a narrower forward scattering lobe, and therefore weaker scattering at intermediate angles (80–200” in Fig. 3). At large angles $\Theta \gtrsim 500''$ the BA, BAM1, and BAM2 clusters in Fig. 3 (all composed of the same number N_s of identical spherules) have similar $d\sigma_{\text{scat}}/d\Omega$. For grains with different values of N_s , we checked the scaling laws described in equation (18) and verified that they are obeyed to within a few percent.

In Fig. 4, we include as an example the effective medium theory (EMT) calculation for a grain with the same mass and porosity as a $N_s = 256$, BAM2 aggregate. The EMT calculation approximates the cluster by a uniform density sphere with refractive index $m_{\text{EMT}} = 1 + (1 - \mathcal{P})(m - 1)$. For $\Theta \lesssim \Theta_{\text{char}}$, the EMT and ADT calculations are in agreement. However, EMT does not take into account the substructure of the grain aggregate, which is important for $\Theta \gtrsim \Theta_{\text{char}}$.

We have also used the discrete dipole approximation (Draine & Flatau 1994) to calculate the extinction cross sections for the clusters at the effective wavelengths of the R , V , and B bands ($\lambda = 0.6492, 0.5470$, and $0.4405 \mu\text{m}$), using the public-domain code DDSCAT 7.0 (Draine & Flatau 2008). Results for selected clusters are shown in Table 1, together with the differential cross section for forward-scattering of X-rays.

4. X-RAY SCATTERING DIAGNOSTICS

The scattering angle Θ is related to the observed halo angle Ψ via the relation:

$$d \tan \Psi = (D - d) \tan(\Theta - \Psi), \quad (20)$$

where d and D are the distances to the dust population and X-ray source, respectively. For example, we have $\Psi = \Theta/2$ when $d = D/2$. Generally, we have $\Psi \approx \Theta$ when $d/D \ll 1$ and $\Psi \ll \Theta$ when $d \sim D$.

For $a_{\text{eff}} \gtrsim 0.1 \mu\text{m}$ grains at optical wavelengths, the ratio σ_B/σ_R of extinction in the B - to the R -band is a generally decreasing function of a_{eff} and serves as a diagnostic of the grain size. The observed value of $A_B/A_R \approx 1.689$ for the average interstellar reddening curve with $A_V/E(B-V) \approx 3.1$ (Fitzpatrick 1999) requires viable grain models to have the extinction at optical wavelengths dominated by grains with $\sigma_B/\sigma_R \approx 1.689$. Single-sized spheres with the dielectric function of “astronomical silicate” (Draine 2003) have $\sigma_B/\sigma_R = 1.689$ for radius $a = 0.177 \mu\text{m}$.

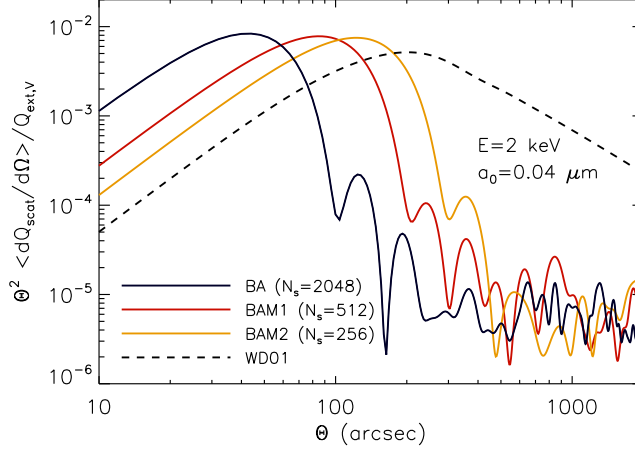


FIG. 6.— $[\Theta^2 dQ_{\text{sca}}(2 \text{ keV})/d\Omega]/Q_{\text{ext}}(V \text{ band})$ for BA.2048.1–3, BAM1.512.1–3 and BAM2.256.1–3 aggregates (with $a_0 = 0.04 \mu\text{m}$) that approximately satisfy $\sigma_B/\sigma_R = 1.689$ (see text). Forward scattering per unit A_V increases with increasing porosity. The result for the WD01 dust model is also shown.

A grain model can be tested by comparison with observed X-ray scattering halos over a range of halo angles. Because calculations of optical-UV extinction and X-ray scattering by complex grain geometries are very time-consuming, it is helpful to have simple diagnostics that can be applied specifically to the grains that dominate the extinction at optical wavelengths, because these same grains are expected to dominate the total X-ray scattering at all except the largest angles. Accordingly, we seek to characterize the X-ray scattering properties of the grain model for scattering angles $\Theta \lesssim \Theta_{\text{char}}(a = 0.2 \mu\text{m}) \approx 407'' (\text{keV}/E)$.

4.1. Core Slope Diagnostic: \mathcal{R}_X

For interstellar dust models based on compact grains, the optical extinction is dominated by grains with radii $R \approx 0.2 \mu\text{m}$, which will have characteristic scattering angles $\Theta_{\text{char}} \approx 200'' (2 \text{ keV}/E)$. For dust at $d/D \approx 0.5$, the characteristic halo angle would be $\Psi_{\text{char}} \approx 0.5 \Theta_{\text{char}}$. Here we devise a diagnostic \mathcal{R}_X that is based on the slope of the scattering halo for $\Psi < \Psi_{\text{char}}$:

$$\mathcal{R}_X(\Psi_1, \Psi_2, \Psi_3, \Psi_4; E_1, E_2) \equiv \frac{\Delta\sigma(\Psi_1, \Psi_2, E_1)}{\Delta\sigma(\Psi_3, \Psi_4, E_2)}, \quad (21)$$

where

$$\Delta\sigma(\Psi_a, \Psi_b, E) \equiv 2\pi \int_{\Psi_a}^{\Psi_b} \frac{d\sigma_{\text{scat}}}{d\Omega}(\Theta, E) \sin \Psi d\Psi. \quad (22)$$

For fixed halo angles $\Psi_1 < \Psi_2 \leq \Psi_3 < \Psi_4$, we have higher values of \mathcal{R}_X for larger grains because of the increased forward scattering. An integral property like \mathcal{R}_X provides a useful comparison between theory and observations because it averages over oscillatory behavior in $d\sigma_{\text{scat}}/d\Omega(\Theta)$ when considering grains of a single size.

For illustration, we set $E_1 = E_2 = 2 \text{ keV}$, and adopt the following halo angles:

$$\begin{aligned} \Psi_1 &= 5'' (\ll \Theta_{\text{char}}) \\ \Psi_2 &= \Psi_3 = 50'' (\approx 0.25 \Theta_{\text{char}}), \\ \Psi_4 &= 100'' (\approx 0.5 \Theta_{\text{char}}) \end{aligned} \quad (23)$$

In Fig. 5, we construct curves of \mathcal{R}_X vs. σ_B/σ_R , for different values of d/D . The grain aggregates considered have $0.25 \lesssim a_{\text{eff}} \leq 0.64 \mu\text{m}$ and $0.33 \lesssim R \lesssim 1.25 \mu\text{m}$. For the calculations in Fig. 5, we have averaged the differential cross sections over three random realizations of the grain aggregates, a process we will incorporate for the rest of the paper.

The vertical dotted line in Fig. 5 is the “observed” value of $\sigma_B/\sigma_R = 1.689$ for dust in the diffuse interstellar medium (ISM) with $R_V \equiv A_V/E(B-V) = 3.1$ (Fitzpatrick 1999). It represents an average over the mixture of grain sizes and composition present in the ISM. For single-size grains with a given porosity, σ_B/σ_R decreases monotonically with increasing size for $\sigma_B/\sigma_R \gtrsim 1.2$. The interstellar grain size distribution extends over a wide range, but the grain size for which $\sigma_B/\sigma_R = 1.689$ will be characteristic of the grains that dominate the extinction in the B -, V - and R -bands.

The computations reported for the aggregates were CPU-intensive, therefore only a limited number of cases could be calculated. In Fig. 6, we show the differential scattering cross section for the BA ($N_s = 2048$), BAM1 ($N_s = 512$) and BAM2 ($N_s = 256$) grains that approximately satisfy the $\sigma_B/\sigma_R = 1.689$ constraint. We compare these calculations to the scattering properties of the WD01 dust model.

\mathcal{R}_X can be calculated for any grain model. However, grain models that are incompatible with the observed interstellar reddening law are of no interest. Restricting ourselves to aggregates that satisfy $\sigma_B/\sigma_R = 1.689$ determines N_s for our chosen value of $a_0 = 0.04 \mu\text{m}$.

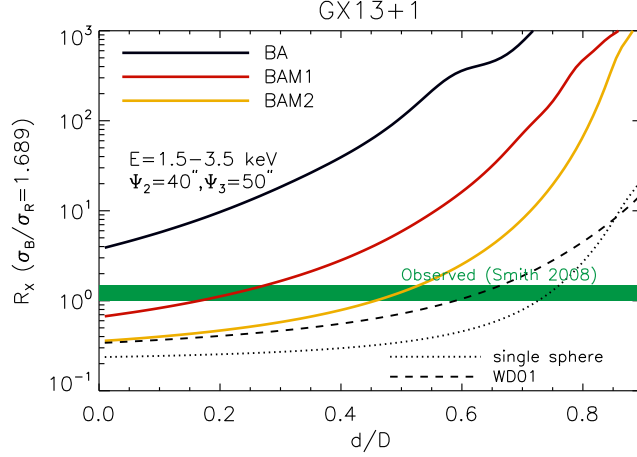


FIG. 7.— Observed and theoretical \mathcal{R}_X vs. the ratio of the distances to the dust population and GX13+1. The width of the “observed” band reflects uncertainties in using both the HRC-I and ACIS-I data to evaluate $\Delta\sigma$ ($50''$, $100''$, E).

We compare our results in Fig. 5 to calculations for single astronomical silicate spheres with radii of $a = 0.1\text{--}0.3\ \mu\text{m}$. The characteristic grain radius that satisfies $\sigma_B/\sigma_R = 1.689$ is $a = 0.177\ \mu\text{m}$. We also show \mathcal{R}_X calculated for the WD01 size distributions for carbonaceous (including polycyclic aromatic hydrocarbons) and silicate grain populations for sightlines with $R_V = 3.1$. For $d/D \leq 0.9$, our single sphere calculations *underestimate* the \mathcal{R}_X values calculated for the WD01 size distributions, though by only $\sim 33\%$ on average.

Another issue to address is the grain composition adopted. We have neglected carbonaceous material, because the volume of silicate material is ~ 1.5 times the volume of carbonaceous solids. Moreover, the silicates are more effective for X-ray scattering at $E > 1\ \text{keV}$ because $|m - 1|$ is larger than for graphite (see Figs. 3 and 5 of Draine [2003]). At $E = 2\ \text{keV}$, $|m - 1| = 1.94 \times 10^{-4}$ for MgFeSiO_4 versus 1.13×10^{-4} for graphite; the scattering power scales as $|m - 1|^2$. Therefore, the graphite grains make only a secondary contribution to the scattering at $E > 1\ \text{keV}$.

4.2. Core X-Ray Scattering per A_V Diagnostic: \mathcal{T}_X

We construct a second diagnostic based on the strength of the X-ray scattering in the “core” relative to the optical extinction. Define

$$\begin{aligned} \mathcal{T}_X &\equiv \left(\frac{D}{D-d} \right)^2 \frac{\Delta\tau_{\text{scat}}(\Psi_1, \Psi_2, E)}{A_V} \\ &= 0.92 \left(\frac{D}{D-d} \right)^2 \frac{\Delta\sigma(\Psi_1, \Psi_2, E)}{\sigma_V}, \end{aligned} \quad (24)$$

where $\Delta\tau_{\text{scat}} = (n_d/n_H)N_H\Delta\sigma$, (n_d/n_H) is the number of dust grains per H nucleon, N_H is the column density, and $\Delta\sigma$ is defined in equation (22). \mathcal{T}_X can be calculated for any mixture of grains, but we are again only interested in grain models that are compatible with the observed interstellar reddening law. The forward-scattering cross section is strongly dependent on the grain size, and therefore this diagnostic is sensitive to the presence of larger grains in the size distribution.

4.3. Comparison to Measured Dust Haloes

The \mathcal{R}_X and \mathcal{T}_X diagnostics constructed in §§4.1, 4.2 allow us to compare our theory with observations of X-ray dust haloes. Recently, high-precision *Chandra* observations of scattered haloes around X-ray binaries have allowed for detailed comparisons to grain models (S08; Thompson & Rothschild 2009). S08 gives a flavor of the technical difficulty of the X-ray background subtraction involved in measuring the dust halo around the Galactic binary GX13+1 using HRC-I and ACIS-I. The HRC-I data is measured for $2'' \lesssim \Psi \lesssim 786''$, while the ACIS-I data is for $50'' \lesssim \Psi \lesssim 989''$. S08 noted the good level of agreement between the HRC-I and ACIS-I data between $50''$ and $100''$. Uncertainties with background subtraction make it difficult to study X-ray halos at large halo angles ($\Psi \gtrsim 500''$). At small angles ($\Psi \lesssim 5''$), it becomes difficult to untangle the halo signal from the instrumental point spread function (resulting from, e.g., micro-roughness of the telescope mirror).

The range of halo angles available in the GX13+1 measurement makes it an ideal case study for us. However, the HRC-I count rate is dominated by the point-spread function (PSF) for $\Psi \gtrsim 200''$ (see §3 of S08) and the measured PSF provided to us by R.K. Smith (2008, private communication) in electronic form only extends up to about $180''$. Since the HRC-I has no energy resolution, S08 used the best-fit model for the measured *RXTE* PCA spectrum of GX13+1 and folded it through the HRC-I response function (see Fig. 3 of S08). We compute the effective $\Delta\sigma(\Psi_1, \Psi_2, E)$ by

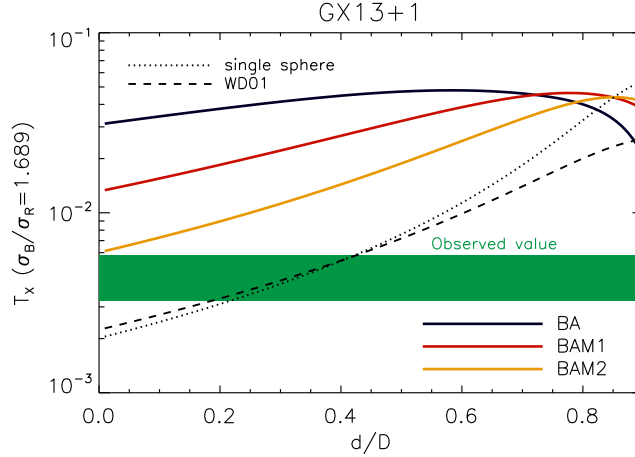


FIG. 8.— Observed and theoretical \mathcal{T}_X vs. the ratio of the distances to the dust population and GX13+1. The width of the “observed” band reflects uncertainties in A_V .

taking an average over the energy spectrum of detected counts:

$$\overline{\Delta\sigma}(\Psi_1, \Psi_2, E) = \sum_{j=1}^4 W_{E_j} \Delta\sigma(\Psi_1, \Psi_2, E_j), \quad (25)$$

where the index j runs over $E_j = 1.75\text{--}3.25$ keV in intervals of $\Delta E = 0.5$ keV. The characteristic energy is then $\bar{E} \approx 2.5$ keV; we set $\Psi_1 = 4''$ and $\Psi_2 = 40''$. The weights are

$$W_{E_j} = \frac{\int_{E_j - \Delta E/2}^{E_j + \Delta E/2} N_E dE}{\int_E N_E dE}, \quad (26)$$

where N_E is the energy spectrum of detected counts. Similarly, we compute $\overline{\Delta\sigma}(\Psi_3, \Psi_4, E)$ by taking $\Psi_3 = 50''$ and $\Psi_4 = 100''$. Using $\overline{\Delta\sigma}(\Psi_1, \Psi_2, E)$ and $\overline{\Delta\sigma}(\Psi_3, \Psi_4, E)$, we construct theoretical values of \mathcal{R}_X in Fig. 7.

Using the HRC-I and ACIS-I data and the stated halo angles yields the measured value of $\mathcal{R}_{X,\text{obs}} = 1.26 \pm 0.25$. The theoretical value depends on the assumed value of d/D . From Fig. 7, we see that the BA model appears to be ruled out by the \mathcal{R}_X test. The BAM1 and BAM2 models are compatible with the \mathcal{R}_X test for $d/D \approx 0.25$ and 0.5 , respectively.

We show theoretical values of \mathcal{T}_X in Fig. 8. To obtain $\mathcal{T}_{X,\text{obs}}$, we need A_V . Ueda et al. (2004) measured the column density along the line of sight to GX13+1 to be $N_H = (3.2 \pm 0.2) \times 10^{22} \text{ cm}^{-2}$. Since GX13+1 is located towards the inner galaxy, we assume A_V/N_H to be 1.25 ± 0.25 times the local value ($4.65 \times 10^{-22} \text{ mag cm}^2$; Rachford et al. 2009) and obtain $A_V = 18.6 \pm 3.9$, somewhat larger than earlier estimates $A_V = 10.2 \pm 0.3$ (Garcia et al. 1992) and $A_V = 15.4 \pm 2.2$ (Charles & Naylor 1992). The observed value $\mathcal{T}_{X,\text{obs}} = 0.0046 \pm 0.0013$ is inconsistent with the BA and BAM1 models for all values of d/D , but may be marginally compatible with the BAM2 model provided $d/D \lesssim 0.1$. However, it is clear that the large extinction toward GX13+1 is not located at $d/D \approx 0$, but instead almost certainly arises mainly in the 3.5 kpc ring at $d \approx 5$ kpc where the Norma and Crux-Scutum arms cross the sightline to GX13+1. Therefore we conclude that all 3 fluffy-grain models – BA ($\mathcal{P} \approx 0.87$), BAM1 ($\mathcal{P} \approx 0.73$), and BAM2 ($\mathcal{P} \approx 0.57$) – are ruled out by $\mathcal{T}_{X,\text{obs}}$ toward GX13+1. Based on both diagnostics, the porosity of interstellar dust is $\mathcal{P} \lesssim 0.55$.

What do the \mathcal{R}_X and \mathcal{T}_X diagnostics say about compact grain models? The WD01 model, based on a mixture of compact silicate and carbonaceous grains, reproduces $\mathcal{R}_{X,\text{obs}}$ if $d/D \approx 0.60 - 0.65$, but reproduces $\mathcal{T}_{X,\text{obs}}$ only if $d/D \approx 0.2 - 0.4$. In reality, the dust is presumably distributed along the sightline to GX13+1 rather than residing in a single cloud. From the variation of \mathcal{T}_X with d/D in Fig. 8 it is clear that WD01 dust uniformly-distributed along the sightline would result in a \mathcal{T}_X value considerably larger than $\mathcal{T}_{X,\text{obs}}$, consistent with the conclusion of Smith (2008) who found that smoothly-distributed WD01 model dust would approximately reproduce the observed X-ray scattering only if $N_H \approx (1.5 - 2) \times 10^{22} \text{ cm}^{-2}$, well below $N_H \approx 3.2 \times 10^{22} \text{ cm}^{-2}$ estimated by Ueda et al. (2004). This may indicate that the WD01 dust model produces too much X-ray scattering. However, (1) there may be systematic errors in the modeling introduced by the broad spectrum of X-ray energies contributing to the HRC-I imaging, and (2) the effects of multiple scattering are not negligible at the lowest energies. In addition, the estimate of A_V is based on X-ray absorption along the line of sight to GX13+1, whereas the X-ray scattering at $300''$ is produced by dust that may be displaced from the line of sight by up to ~ 10 pc. Perhaps A_V on the direct sightline to GX13+1 is larger than the average dust column contributing to the scattered halo. For example, if the dust producing the scattering halo toward GX13+1 had $A_V \approx 12 \pm 3$ rather than 18.6 ± 3.9 , the “observed” band in Fig. 8 would shift upward by about a factor of 1.55, and the WD01 model would be more-or-less consistent with both $\mathcal{R}_{X,\text{obs}}$ and $\mathcal{T}_{X,\text{obs}}$ for $d/D \approx 0.55$. Compact grain models therefore appear to be viable, whereas all three of the fluffy grain models considered here appear to be

TABLE 1
OPTICAL EXTINCTION AND X-RAY FORWARD SCATTERING FOR SELECTED TARGETS

target	\mathcal{P}	a_{eff} (μm)	R (μm)	Q_{ext} R	Q_{ext} V	Q_{ext} B	$(dQ_{\text{sca}}/d\Omega)_0$ 2 keV
BA.2048.1	0.8644	0.508	0.989	4.986	6.484	8.352	3.353×10^6
BA.2048.2	0.8657	0.508	0.992	4.958	6.460	8.370	3.384×10^6
BA.2048.3	0.8651	0.508	0.990	5.004	6.502	8.392	3.364×10^6
BAM1.512.1	0.7239	0.320	0.491	3.358	4.425	5.764	5.319×10^5
BAM1.512.2	0.7530	0.320	0.510	3.211	4.308	5.749	5.326×10^5
BAM1.512.3	0.7286	0.320	0.494	3.331	4.398	5.789	5.279×10^5
BAM2.256.1	0.5632	0.254	0.335	2.877	3.771	4.877	2.116×10^5
BAM2.256.2	0.5781	0.254	0.339	2.841	3.736	4.822	2.103×10^5
BAM2.256.3	0.5818	0.254	0.340	2.807	3.732	4.857	2.085×10^5
sphere	0	0.177	0.177	2.499	2.940	4.227	5.012×10^4

All targets consist of astronomical silicate (Draine 2003).

firmly ruled out by the \mathcal{T}_X diagnostic.⁴

5. DISCUSSION

We have shown how the global structure of porous dust grain agglomerates leads to increased X-ray scattering at small angles, when compared with the scattering properties of spherical grains (both single size and the WD01 size distribution) that are constrained to have the observed ratio of extinction in the B and R bands. The enhanced small-angle scattering implies that observations of scattered X-ray halos can be used to constrain the internal geometry of interstellar grains. Applying the \mathcal{R}_X and \mathcal{T}_X diagnostics described above, we find that the observed X-ray halo around GX13+1 is inconsistent with grains consisting of random aggregates with porosities $\mathcal{P} \gtrsim 0.55$, at least for the monomer sizes considered here ($a_0 = 0.04 \mu\text{m}$).

Smith et al. (2002) argued that the dust toward GX13+1 could not consist of porous grains, on the grounds that porous grains could not produce sufficient overall scattering. Our \mathcal{T}_X diagnostic uses the strength of the “core” of the scattered halo to constrain the dust porosity, but now we use the fact that porous grains would produce *too much* small-angle scattering per unit A_V .

This exploratory study has focused on the X-ray scattering properties of only the grains that dominate the optical extinction, with the expectation that these are representative. Future studies should:

1. Use size distributions of grain aggregates (adjusted to reproduce the full extinction curve and not just A_B/A_R) rather than just averaging over random realizations of a single aggregate size as was done here. We have shown that the \mathcal{R}_X and \mathcal{T}_X diagnostics for single-size silicate spheres with $\sigma_B/\sigma_R = 1.69$ provide a good approximation to \mathcal{R}_X and \mathcal{T}_X calculated for the full WD01 size distribution, so we are confident that using single-size fluffy grains with $\sigma_B/\sigma_R \approx 1.69$ provides a reasonable approximation to what \mathcal{R}_X and \mathcal{T}_X would be for size distributions constrained to reproduce the observed extinction curve. Nevertheless, \mathcal{R}_X , in particular, will change when the single “representative” grain size is replaced by a size distribution that reproduces the IR-UV extinction curve. The \mathcal{T}_X diagnostic is expected to be more robust, because the grains that dominate the visual extinction are also expected to dominate the scattering at $\Theta < \Theta_{\text{char}}$ ($R = 0.2 \mu\text{m}$).
2. Include carbonaceous material, even though that material contributes only $\sim 40\%$ of the total grain volume. Again, we have already tested for sensitivity to the carbonaceous component by showing that \mathcal{R}_X and \mathcal{T}_X for single-size silicate spheres approximates \mathcal{R}_X and \mathcal{T}_X for the full WD01 size distribution, including carbonaceous grains, but it would be best to explicitly consider fluffy grain models that include a carbonaceous component.
3. Examine the effect of varying the monomer size. The monomer size used in the present work ($0.040 \mu\text{m}$) was chosen arbitrarily. While we expect that similar results will be obtained for monomer sizes $a_0 \gtrsim 0.010 \mu\text{m}$, this remains to be verified by future (numerically challenging) calculations.

Although confirmation by more extensive future studies (as discussed above) will be invaluable, the diagnostics developed here, in particular the \mathcal{T}_X diagnostic, already demonstrate that the dust toward GX13+1 has porosity $\mathcal{P} \lesssim 0.55$. This finding appears to rule out models (e.g., Mathis & Whiffen 1989; Voshchinnikov et al. 2006) in which the interstellar grain mixture is dominated by highly-porous aggregates with $\mathcal{P} \gtrsim 0.8$.

The porosity of interstellar dust grains therefore appears to be *lower* than the porosity of the submicron grains in the debris disk around AU Mic, which (based on interpretation of observed polarized scattering) have $\mathcal{P} \approx 0.6$, or micron-sized cometary dust grains, which also appear to have $\mathcal{P} \approx 0.6$ (Shen et al. 2009, and references therein).

Why interstellar grains are *not* highly-porous is an open question. Gyroresonant acceleration by MHD turbulence in diffuse clouds appears able to drive $a \gtrsim 0.1 \mu\text{m}$ grains to velocities $\sim 1 \text{ km s}^{-1}$ (Yan et al. 2004). Grain-grain collisions at relative velocities $\sim \text{km s}^{-1}$ will likely shatter high-porosity aggregates, and thereby limit the abundance of fragile high-porosity aggregates in the ISM.

⁴ If $A_V \approx 10$, the BAM2 model would be allowed by the \mathcal{T}_X diagnostic if $d/D \lesssim 0.24$, but the \mathcal{R}_X diagnostic requires $d/D \approx 0.50$, so the BAM2 model would remain incompatible with the observational constraints.

K.H. acknowledges generous support by the Institute for Advanced Study, especially for the use of the computing cluster that served as the untiring workhorse for this project. B.T.D. acknowledges partial support by NSF grant AST 0406883. We thank Mario Juric for helpful technical advice, Bernd Aschenbach for an illuminating conversation about X-ray mirrors, and Randall Smith for providing us with his dust halo measurements in an electronic form.

REFERENCES

- Arfken, G.B., & Weber, H.J. 1995, *Mathematical Methods for Physicists*, 4th Edition (San Diego: Academic Press)
- Charles, P.A., & Naylor, T. 1992, *MNRAS*, 255, 6
- Draine, B.T. 1988, *ApJ*, 333, 848
- Draine, B.T. 2003, *ApJ*, 598, 1026
- Draine, B.T., & Allaf-Akbari, K. 2006, *ApJ*, 652, 1318 [DA06]
- Draine, B.T., & Flatau, P.J. 1994, *J. Opt. Soc. Am. A*, 11, 1491
- Draine, B.T., & Flatau, P.J. 2008, <http://arXiv.org/abs/0809.0337>
- Draine, B.T., & Fraisse, A.A. 2009, *ApJ*, 696, 1
- Draine, B.T., & Lee, H.-M. 1984, *ApJ*, 285, 89
- Draine, B.T., & Li, A. 2007, *ApJ*, 657, 810
- Draine, B.T., & Tan, J.C. 2003, *ApJ*, 594, 347
- Fitzpatrick, E.L. 1999, *PASP*, 111, 63
- Garcia, M.R., et al. 1992, *AJ*, 103, 1325
- Kim, S.-H., & Martin, P.G. 1995, *ApJ*, 444, 293
- Kim, S.-H., Martin, P.G., & Hendry, P.D. 1994, *ApJ*, 422, 164
- Mathis, J.S., Ruml, W., & Nordsieck, K.H. 1977, *ApJ*, 217, 415
- Mathis, J.S., & Whiffen, G. 1989, *ApJ*, 341, 808
- Press, W.H., Teukolsky, S.A., Vetterling, W.T., & Flannery, B.P. 1996, *Numerical Recipes in Fortran 90*, Second Edition (New York: Cambridge)
- Rachford, B.L., et al. 2009, *ApJS*, 180, 125
- Shen, Y., Draine, B.T., & Johnson, E.T. 2008, *ApJ*, 689, 260 [SDJ08]
- Shen, Y., Draine, B.T., & Johnson, E.T. 2009, *ApJ*, 696, 2126
- Smith, R.K. 2008, *ApJ*, 681, 343 [S08]
- Smith, R.K., Edgar, R.J., & Shafer, R.A. 2002, *ApJ*, 581, 562
- Thompson, T.W.J., & Rothschild, R.E. 2009, *ApJ*, 691, 1744
- Ueda, Y., Murakami, H., Yamaoka, K., Dotani, T., & Ebisawa, K. 2004, *ApJ*, 609, 325
- van de Hulst, H.C. 1957, *Light Scattering by Small Particles* (New York: Wiley)
- Voshchinnikov, N.V., Il'in, V.B., Henning, T., & Dubkova, D.N. 2006, *A&A*, 445, 167
- Weingartner, J.C., & Draine, B.T. 2001, *ApJ*, 548, 296 [WD01]
- Yan, H., Lazarian, A., & Draine, B.T. 2004, *ApJ*, 616, 895